ADVANCED
FUNCTIONAL
MATERIALS

Supporting Information

for *Adv. Funct. Mater.,* DOI: 10.1002/adfm.201902656

Charge-Carrier Dynamics, Mobilities, and Diffusion Lengths of 2D–3D Hybrid Butylammonium–Cesium–Formamidinium Lead Halide Perovskites

*Leonardo R. V. Buizza, Timothy W. Crothers, Zhiping Wang, Jay B. Patel, Rebecca L. Milot, Henry J. Snaith, Michael B. Johnston, and Laura M. Herz**

Supporting Information

Charge-carrier dynamics, mobilities and diffusion lengths of 2D-3D heterostructured butylammonium-caesium-formamidinium lead halide perovskites

*Leonardo R. V. Buizza, Timothy W. Crothers, Zhiping Wang, Jay B. Patel, Rebecca L. Milot, Henry J. Snaith, Michael B. Johnston, Laura M. Herz**

A. Sample Preparation

We first prepare $FA_{0.83}Cs_{0.17}Pb(I_{0.6}Br_{0.4})_3$ precursor solution by dissolving formamidinium iodide (FAI; Dyesol), caesium iodide (CsI; Alfa Aesar), lead iodide (PbI_2; TCI) and lead bromide ($PbBr_2$; TCI) in anhydrous N,N-dimethylformamide (DMF; Sigma-Aldrich) to obtain a stoichiometric solution. The solution was then stirred overnight in a nitrogen-filled glovebox.

We then add 69 µl of hydroiodic acid (HI; Sigma-Aldrich), 57 wt% in H_2O and 34.6 µl of hydrobromic acid (HBr; Sigma-Aldrich), 48 wt% in H_2O into 1 ml of 1.2 M $FA_{0.83}Cs_{0.17}Pb(I_{0.6}Br_{0.4})_3$ precursor solution, and age for approximately 48 hours under a nitrogen atmosphere without stirring.

In parallel, we generate $BAPb(I_{0.6}Br_{0.4})_3$ precursor solution by dissolving n-butylammonium iodide (BAI; Dyesol), PbI_2 and $PbBr_2$ in DMF to obtain a stoichiometric solution. The solution was also stirred overnight in a nitrogen-filled glovebox.

Prior to film deposition, we blend the $FA_{0.83}Cs_{0.17}Pb(I_{0.6}Br_{0.4})_3$ and $BAPb(I_{0.6}Br_{0.4})_3$ precursor solutions to achieve $BA_x(FA_{0.83}Cs_{0.17})_{1-x}Pb(I_{0.6}Br_{0.4})_3$ with desired BA contents.

The precursor perovskite solution was spin-coated in a nitrogen-filled glovebox at 2000 rpm for 45s, on a substrate pre-heated at 80°C. The films were dried inside the glovebox on a hot plate at a temperature of 70 °C for 60 seconds. The films were then immediately transferred into an oven and annealed in air at 175°C for 80 minutes.

B. Experimental Details

UV-vis. and Infra-Red Absorption

Visible absorption spectra were taken using a Bruker Vertex 80v Fourier-Transform Infrared (FTIR) spectrometer, with a tungsten halogen source and a silicon diode detector. Measurements were carried out under low vacuum (< 5 mbar). Infra-Red absorption measurements were taken using the same FTIR spectrometer fitted with a attenuated total reflection (ATR) accessory. A globar light source was used with a nitrogen-cooled photovoltaic HgCdTe detector. Measurements were taken with samples placed in air.

X-Ray Diffraction

X-Ray Diffraction patterns were measured using a Panalytical X'Pert powder diffractometer, using radiation from a Cu-$K_{\alpha 1}$ source, across 2θ values ranging from 10-45°.

Steady-State Photoluminescence and Segregation Measurements

Photoluminescence (PL) spectra were measured following excitation by a 400 nm continuous wave laser (Picoquant, LDH-D-C-405M). The PL emitted was collected and coupled into a grating spectrometer (Princeton Instruments SP-2558), after which light was detected by an iCCD camera (PI-MAX4, Princeton Instruments). For the PL segregation measurements, the same setup was used, with PL spectra being measured after 1, 10, 30, 60, 120, and 300 s. Measurements were carried out in air.

Time-Correlated Single Photon Counting

The same laser as above was used to photoexcite the thin films from the front side of the perovskite film (not facing the substrate), but under pulsed excitation mode. A repetition rate of 1MHz was used for all measurements. Photoluminescence (PL) was collected using the same monochromator, with a photon-counting detector (PDM series from MPD). Timing is controlled electronically using a PicoHarp300 event timer. PL decays were measured at the initial peak wavelengths. Measurements were carried out in air.

Optical-Pump Terahertz Probe Spectroscopy

An amplified laser system (Spectra Physics, MaiTai – Ascend – Spitfire), with a 5 kHz repetition rate, centre wavelength of 800 nm and pulse duration of 35 fs was used to generate THz radiation via the inverse-spin Hall effect from an emitter made of 2nm of tungsten / 1.8nm of $Co_{40}Fe_{40}B_{20}$ / 2nm of platinum, supported by a quartz substrate.[1] The THz probe was focused onto the sample and detected via free-space electro-optical sampling in a ZnTe(110) crystal of thickness 200 µm. A 400 nm pump pulse was generated using a Beta Barium Borate (BBO) crystal. Transient decays were measured by recording the change in peak THz amplitude transmitted as a function of pump-probe delay time. Measurements were carried out under vacuum (< 10^{-2} mbar).

C. Absorption and Photoluminescence Spectra

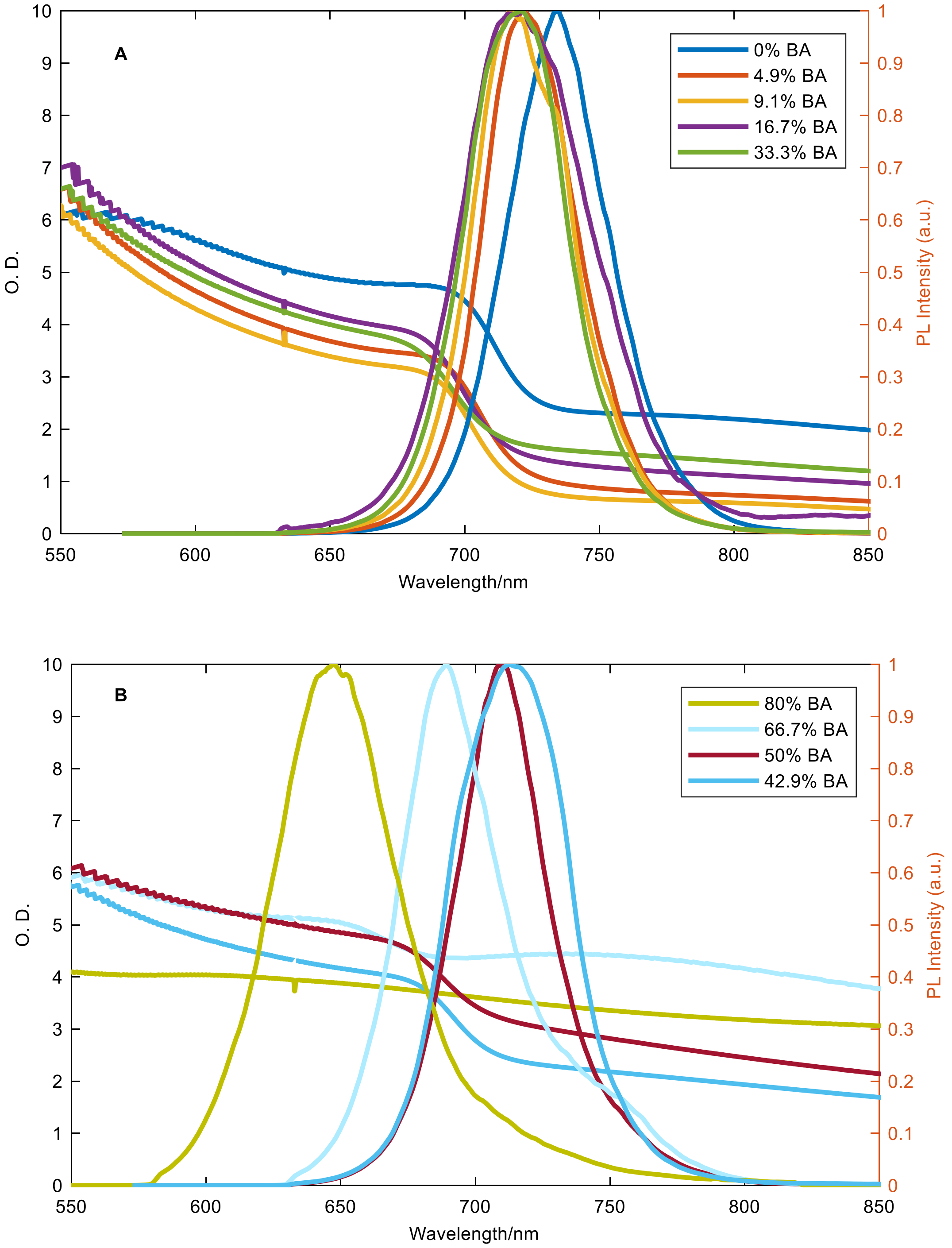

Figure S1: Steady-state photoluminescence (PL) and absorption spectra for thin films of BA$_x$(FA$_{0.83}$Cs$_{0.17}$)$_{1-x}$Pb(I$_{0.6}$Br$_{0.4}$)$_3$ for x = 0 – 0.333 (A) and x = 0.429 – 0.8 (B). PL was measured following continuous-wave excitation at 400nm at an intensity of 122 mWcm^{-2} on the front of the samples. All of the films had thicknesses greater than 700 nm, well above the optical absorption depth at 400 nm. The absorption onset and PL peak both blue-shift with increasing BA content.

The trends seen here in band gap energy, with band gap increasing with BA content, must be married with the reduced interplanar spacing that is determined from XRD measurements (see below). The dependence of band gap energy on lattice spacing is not trivial, with several contributing factors. It is now well understood that the nature of the band gap in $MAPbI_3$ is governed by the overlap of the B- and X-site orbitals: the Valence Band Maximum (VBM) arises from the antibonding states of Pb 6s and I 5p, and the Conduction Band Minimum (CBM) is formed by empty Pb 6p orbitals or Pb 6p – I 5p interactions.[2,3] This electronic structure is inverted relative to classical inorganic semiconductors, such as GaAs, leading to lead halide perovskites having a positive deformation potential.[4–6] This has been confirmed by pressure-dependent measurements in $MAPbBr_3$, where increasing pressure in the cubic phase leads to shorter Pb-Br bond lengths, raising the VBM and leaving the CBM unchanged, giving a smaller band gap[7]. However, if the A-site cation is varied, there is a non-obvious relationship between the size of the cation and the band gap. One would expect smaller cations to lead to decreased interatomic spacing, thus giving smaller band gaps. However, a crucial factor is the metal-halide bond angle, meaning that larger ionic radii give larger angles, lining up the metal-halide bonds, giving lower band gaps[8,9]. Thus, for example, swapping MA for FA leads to a lower band gap in $FAPbI_3$.[10]

Temperature-dependent measurements have further probed this relationship, with previous studies showning that the band gap of MHPs blue-shifts with increasing temperature, and this effect has been found in conventional $MAPbI_3$ as well as mixed-halide and mixed lead-tin perovskites.[11–14] When considering the effect of temperature, there are contributions from both lattice deformation and electron-phonon coupling.[15] There is debate as to the dominance of the contributions: early work suggested that the electron-phonon couplings might cancel each other out, leaving just the lattice expansion contribution.[15] However, more recent work has found a large anharmonicity in electron-phonon couplings,[16] and theoretical calculations have found the dominant increase in band gap to arise from the electron-phonon couplings.[17,18]

By tuning the halide content, we can change the orbital overlap, altering the energy of the VBM whilst leaving the CBM unchanged, due to the large contribution from the halide p-orbital to the VBM.[19] We thus get varying band gap energy with halide content, with E_g

decreasing in order of chlorine / bromine / iodine, with mixtures of two halides confirming this trend.[19–21]

The addition of BA to the materials under investigation here leads to lower interatomic spacing,[22] and if this were the only effect, would result in corresponding decrease in the band gap due to the positive deformation potential of MHPs. However, since the PL and absorption show a blue-shift with increasing BA content we thus suggest that the more convincing explanation is of a slight variation in halide content within the 3D bulk region. The presence of a higher bromide fraction within the 3D bulk region of samples with a greater BA content will thus increase the band gap whilst reducing the lattice spacing, which is consistent with the observed trends in both XRD peaks and band gaps.

D. Infra-Red Absorption Spectra

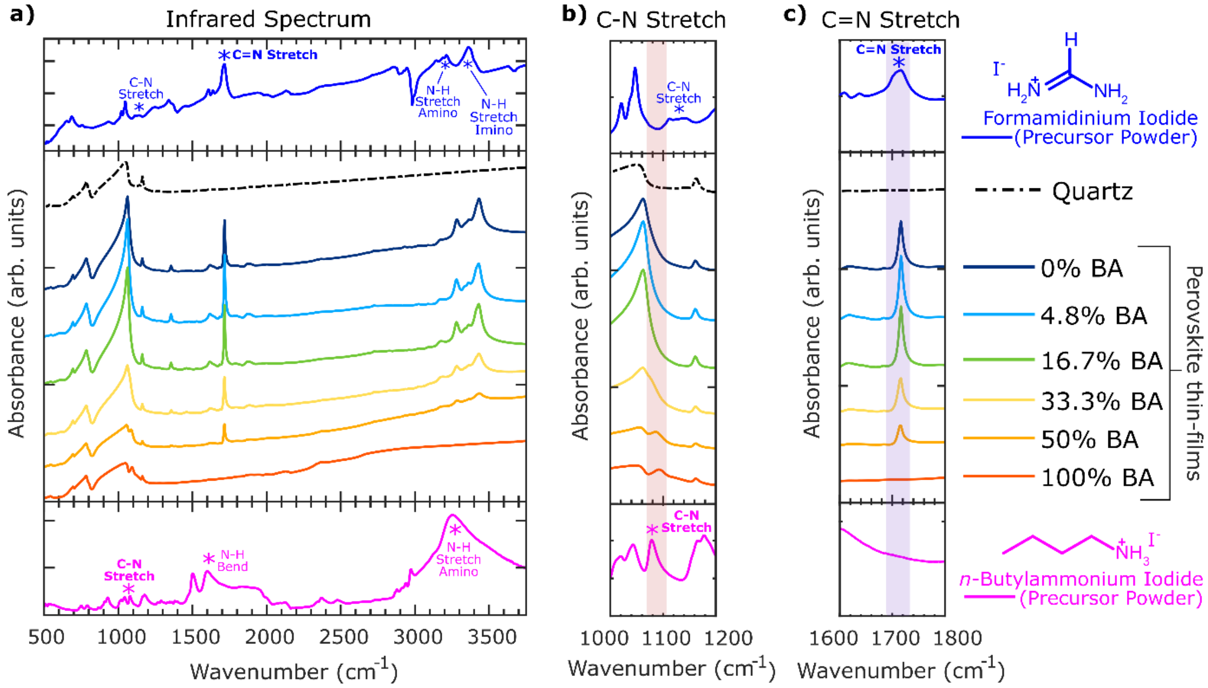

Figure S2: (A) Infrared absorption spectra of $BA_x(FA_{0.83}Cs_{0.17})_{1-x}Pb(I_{0.6}Br_{0.4})_3$ thin films on z-cut quartz obtained using an attenuated total reflection (ATR) accessory mounted within an FTIR instrument. Also shown are the IR spectra of the precursor powders, formamidinium iodide and *n*-butylammonium iodide (blue and pink lines respectively). The peaks were assigned according to relevant references.[23–25] (B) Spectral zoom showing the infrared spectra of the perovskite thin films between 1000 cm^{-1} and 1200 cm^{-1}. The rise in absorption of the C-N stretching mode from the butylammonium cation (BA^+) highlight the increasing BA^+ fraction in the perovskite thin-films. (C) The infrared spectra of the perovskite thin films between 1600 cm^{-1} and 1800 cm^{-1}. The decrease in absorption of the C=N stretching mode (from the formamdinium) highlight the decrease in FA^+ fraction in the perovskite thin-films.

The IR absorption for the C-N stretching frequency associated with n-butylammonium iodide is shifted compared to the formamidinium iodide, as shown in Figure S2. The shift in frequency is due to the R-groups attached to the primary ammonium ion or amine ($BA^+ =$ R - $^+NH_3$, $FA^+ =$ R- NH_2).[26–28] The R-group in BA^+ consists of an aliphatic chain (C_4H_9) whereas the R-group in FA^+ consists of an imino group ($CHNH_2$). The result of the different R-groups is a change in the C-N bond length and bond angle, and will result in a difference in the C-N stretching frequency between the BA^+ and FA^+.[25,26] Using the assigned peaks in the precursor powder, it can be clearly observed that the C-N stretching frequency in the butylammonium cation (BA^+) is 1092 cm^{-1}. The broad peak of the C-N stretching frequency associated with the formamidinium (FA^+) cation is masked by the strong absorption of quartz. Therefore, by tracking the C-N stretching frequency we can monitor the addition of BA^+ in the perovskite thin-film. Further, the vibrational frequencies of bonds associated with the imino group (-C=N-) in the FA^+ at 1716 cm^{-1} and 3433 cm^{-1} are shown to decrease in absorption as the BA^+ fraction is increased in the perovskite. The N-H stretching frequency in the BA^+ is broad, hence it is masked by the increased absorption of the quartz above 3000 cm^{-1}.

E. X-Ray Diffraction

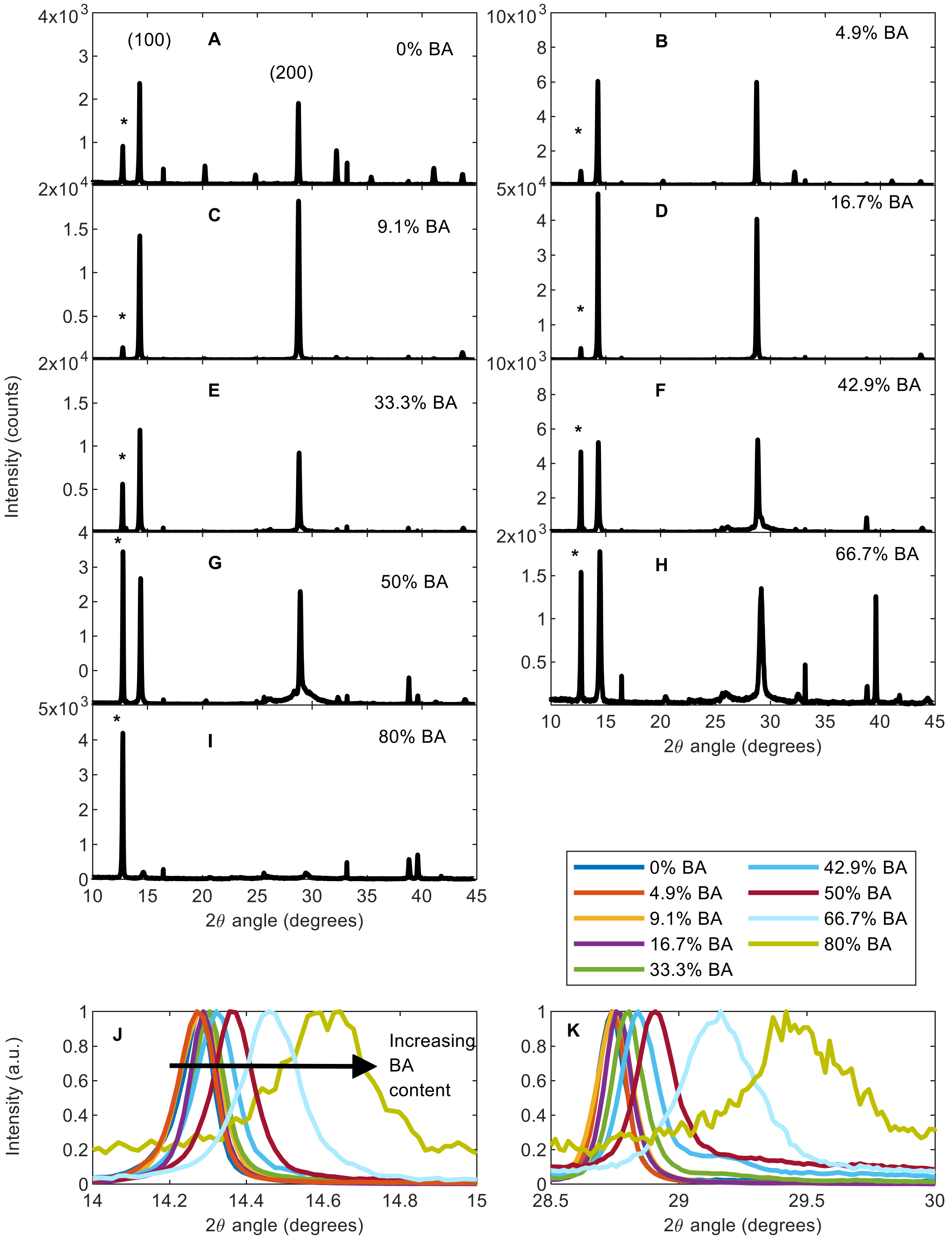

Figure S3: (A) – (I) X-Ray Diffraction spectra for thin films of $BA_x(FA_{0.83}Cs_{0.17})_{1-x}Pb(I_{0.6}Br_{0.4})_3$, for x = 0 – 0.8. Peaks marked with an asterisk (*) are identified as PbI_2 peaks at 12.7°. (J) The main (100) reflection is found at ~14.3° and (K) the (200) reflection is found at ~28.7°. Both peak positions shift to larger angles with increasing BA content.

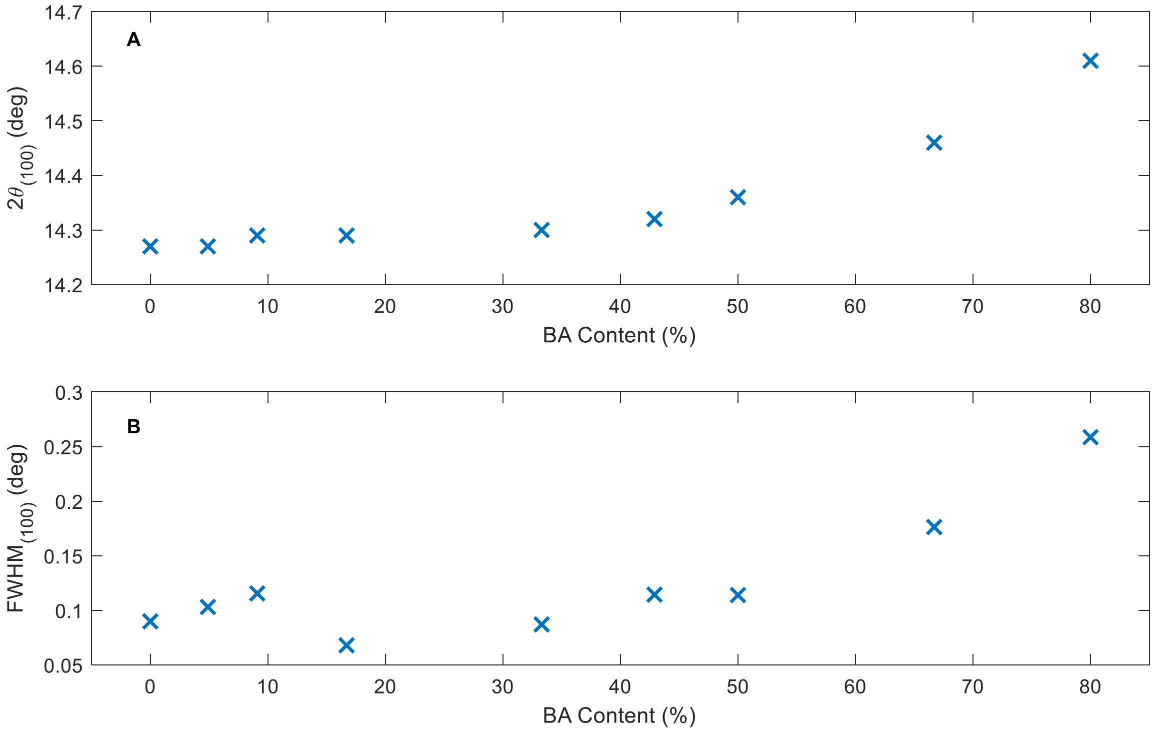

Figure S4: X-Ray Diffraction peak positions for (100) reflections (A) and full-width half-maximum (FWHM) values of the (100) peaks (B). Peak positions and FWHM values both increase with BA content.

Small amounts of BA increase crystallinity, as seen by the increased intensity in (100) and (200) reflections for samples with x = 0.049 – 0.333, and by the lowest full-width half-maximum (FWHM) value for x = 0.167. We also measure increasing reflection angles for the (100) and (200) peaks, implying reduced interplanar spacing. We suggest this is due to two effects: as a larger volume fraction of 2D crystallites forms, increased strain on the 3D bulk lattice causes a reduction in interplanar spacing, and the 3D bulk changes halide composition slightly (see also discussion above and in Main Text), enhancing the iodide content thus again reducing interplanar spacing, leading to larger diffraction angles. These trends are similar to those reported previously by Z. Wang et al.[22] At high BA content (x > 0.5) we see substantial PbI_2 reflections, as well as additional peaks in the spectra. These can be partly attributed to 2D crystallites occupying a significant volume fraction, and also to the lack of fully-formed perovskite phase, with the likely formation instead of a non-stoichiometric phase interspersed throughout the film.

F. PL Stability Measurements

Photostability with respect to aging under inert atmosphere

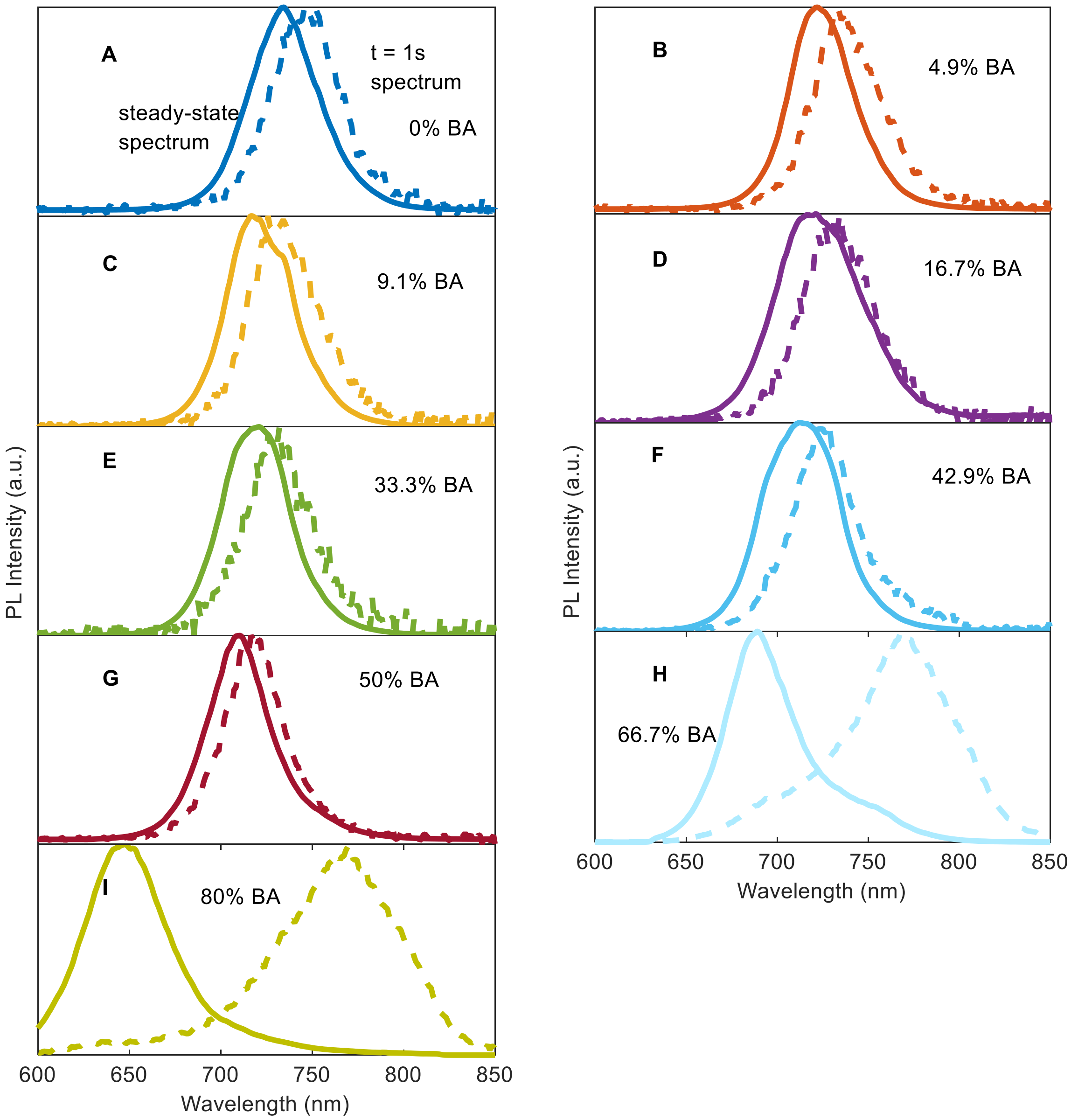

Figure S5: (A) – (I) Photoluminescence spectrum shift between original steady-state PL spectra, and spectra measured for thin films of $BA_x(FA_{0.83}Cs_{0.17})_{1-x}Pb(I_{0.6}Br_{0.4})_3$ following aging in a nitrogen glovebox for three months, for $0 \leq x \leq 0.8$ content (the latter spectra also forming the t = 1s spectra in the PL stability measurements shown in Figure S6).

Photoluminescence Segregation

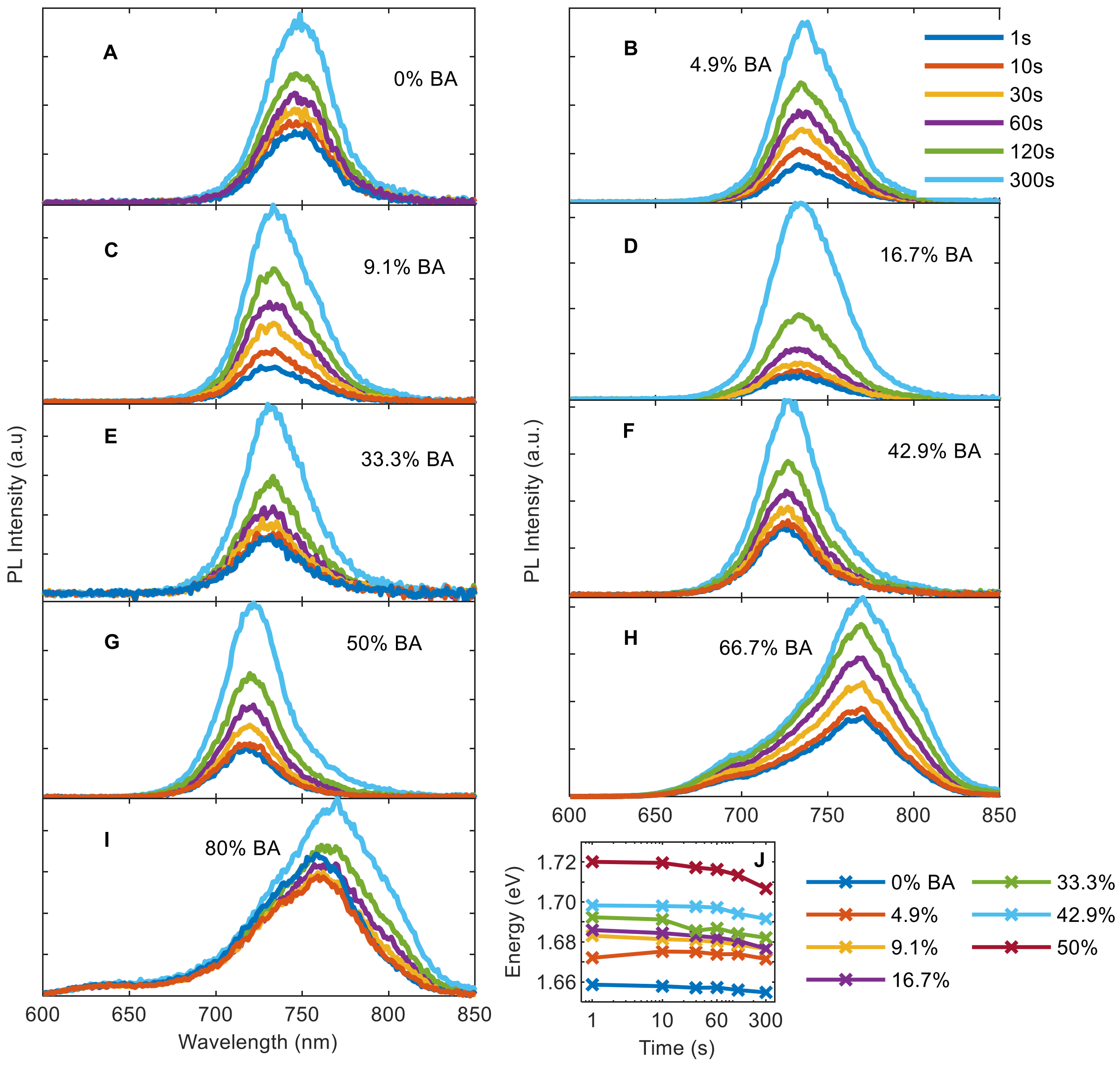

Figure S6: (A) – (I) PL segregation for thin films of $BA_x(FA_{0.83}Cs_{0.17})_{1-x}Pb(I_{0.6}Br_{0.4})_3$ for x = 0 – 0.8 under constant 400nm continuous-wave illumination at approximately one sun intensity (95 mWcm^{-2}). (J) Shift in mean photon energy over 1 – 300 s (see below for details).

For all samples we see that, following aging in a nitrogen glovebox for three months, the PL spectra are red-shifted. This shift is slight for low BA content, but becomes substantial for high BA content, with a secondary peak having formed at ~750 nm, potentially indicative of halide segregation, with the emission now originating from iodide rich domains. These changes are slight for $x \leq 0.5$ where they also do not seem to be associated with the appearance of a secondary peak attributable to a clear iodide rich phase, hence they may be associated with slight morphological or compositional settlement here with time.

We subsequently monitored the stability of the aged films to halide segregation under illumination. We observe increasing PL intensity and a slight red-shift in mean photon energy with time spent under illumination, for all samples, with the amount of red-shift increasing slightly with BA content, as measured by percentage change in mean photon energy after 300s, relative to the initial value, defined as Δ (see below and main text).

We note that since samples with $x = 0.667, 0.8$ had already degraded in the absence of intense light exposure (glovebox light levels) as part of the aging process, shifting most of the PL to a new peak at 750nm, these halide segregation measurements under light are not necessarily indicative of the materials' general propensity to segregate. For this reason, the shifts in E_{phot} are not included in Figure S6 (J) for samples with $x = 0.667, 0.8$.

In order to quantify the amount of segregation undergone by each sample, the mean photon energy of each spectrum was calculated and plotted over time (see Figure S6 (J) and Figure 1 (F) in the Main Text). The iCCD camera is calibrated to a blackbody spectrum with units of energy density, thus the mean photon energy is calculated as:

$$< E_{phot} > \; = \; \frac{Total\ Energy}{N_{Phot}} = \frac{\sum_{i=1}^{N} I_i}{\sum_{i=1}^{N} N_i} = hc\,\frac{\sum_{i=1}^{N} I_i}{\sum_{i=1}^{N} \lambda_i I_i},$$

where I_i are the intensities and λ_i are the corresponding wavelengths at which they are recorded.

G. Transient Photoluminescence Decays

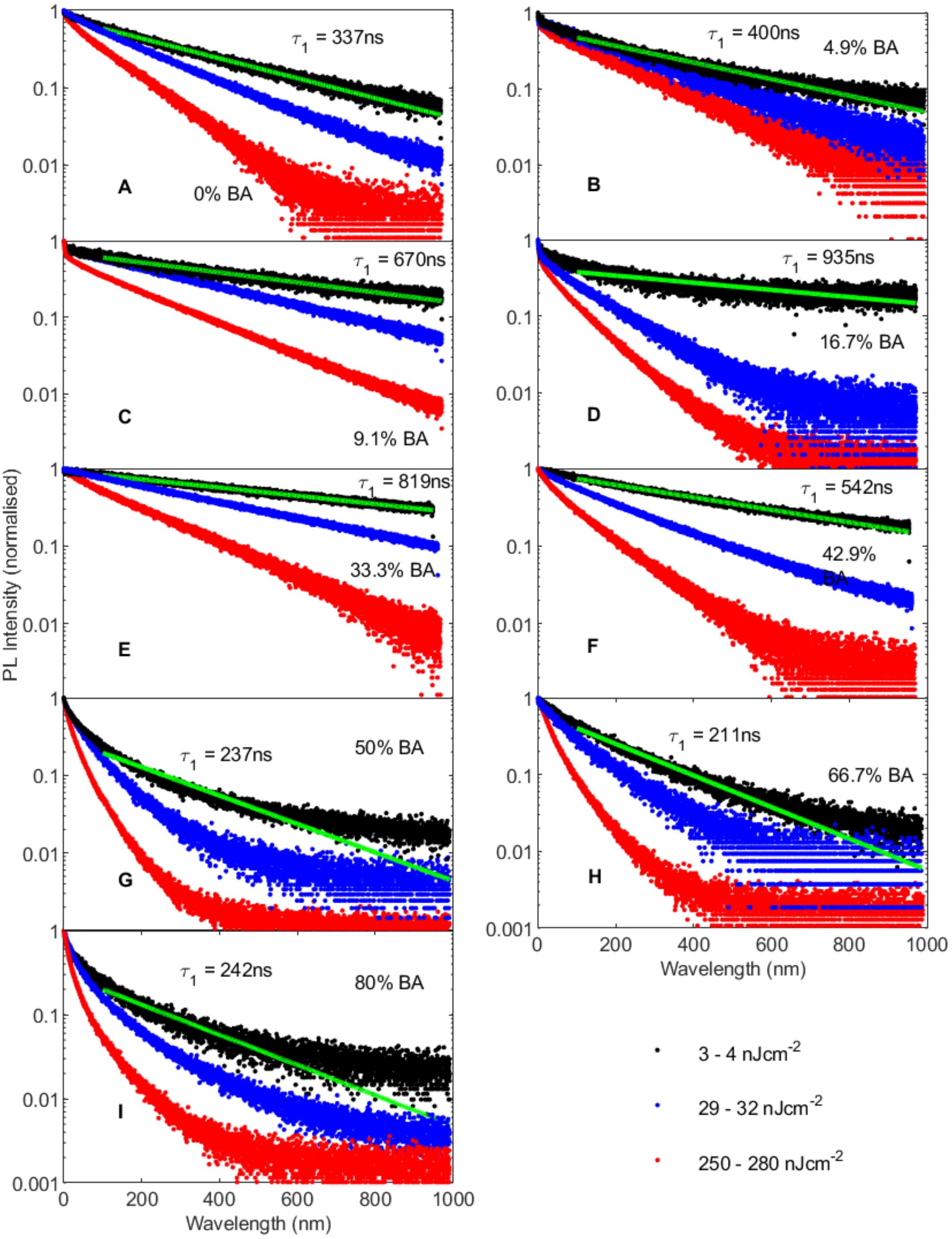

Figure S7: (A) – (I) Transient PL decay curves for a range of excitation fluences for thin films of $BA_x(FA_{0.83}Cs_{0.17})_{1-x}Pb(I_{0.6}Br_{0.4})_3$ for x = 0 – 0.8. Samples were excited at 400nm using fluences of ~4, ~30, ~250 nJcm^{-2}. Decay lifetimes decreased with decreasing fluence, and traces at the lowest fluence were fitted with a monoexponential curve (green) to extract a lifetime τ_1.

H. Terahertz Spectroscopy

Photoconductivity measurements

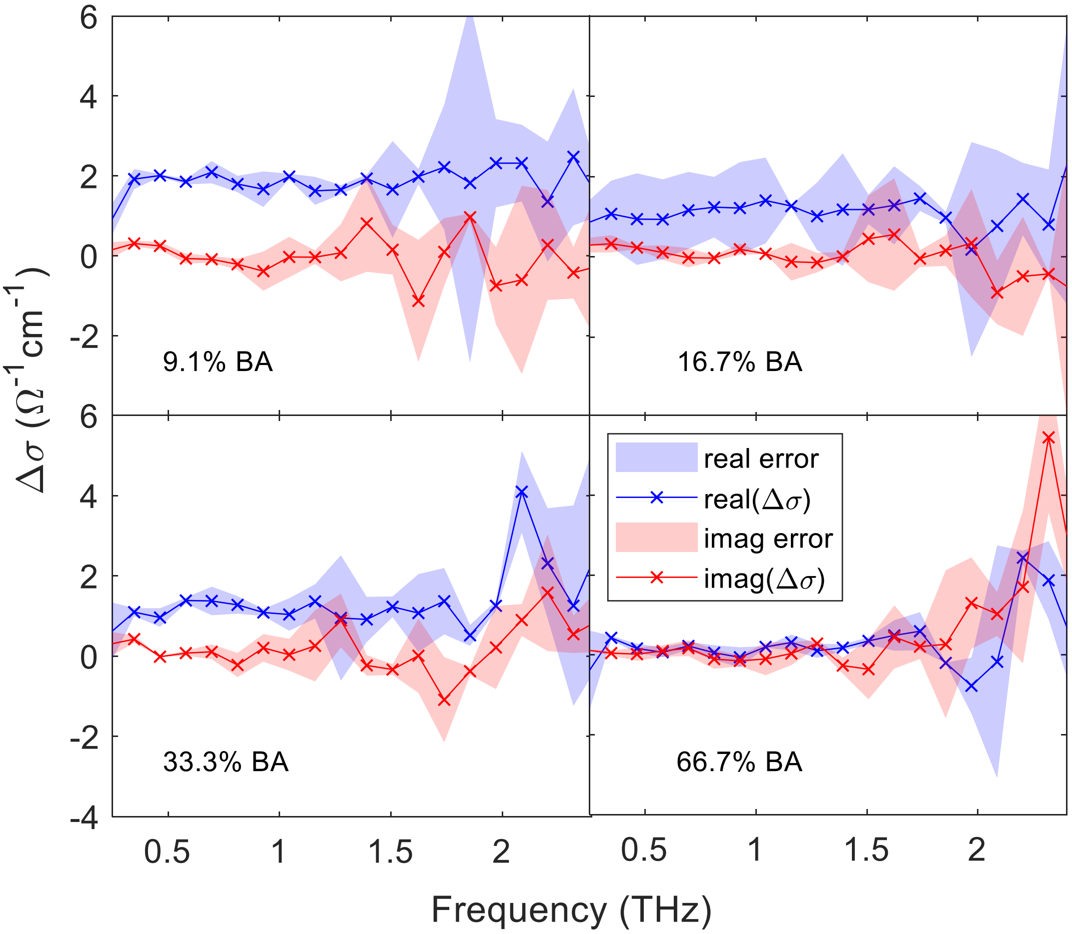

Figure S8: Terahertz photoconductivity spectra measured for thin films of $BA_x(FA_{0.83}Cs_{0.17})_{1-x}Pb(I_{0.6}Br_{0.4})_3$, after 1 ns following excitation at 400nm at a fluence of 1.38 μJcm^{-2}, across four different compositions. Solid lines with crosses are the mean value of two scans, with the shaded area representing the statistical error.

Measurements of the terahertz photoconductivity response were carried out on thin films of $BA_x(FA_{0.83}Cs_{0.17})_{1-x}Pb(I_{0.6}Br_{0.4})_3$, for x = 0.091, 0.167, 0.333, 0.667, after 1 ns following excitation at 400nm at a fluence of 1.38 μJcm^{-2}.

Several studies on a variety of different perovskite compositions have described the nature of excited states in mixed-halide perovskites.[29,30] Given the low exciton binding energy in 3D perovskites,[31,32] and following several studies using photoluminescence, transient absorption and optical-pump, terahertz-probe measurements,[33–36] it is now fairly well-accepted that excited states in 3D perovskites are dominated by free charges, and are well described by the Drude model, with a flat photoconductivity response.[11,37] In thinly-layered 2D layered perovskites with strong electronic confinement, also known as Ruddlesden-Popper perovskites, excitonic and polaronic effects are more common, and these have also been studied in some detail.[38,39] In the 2D-3D hybrid system that we present here, 3D perovskite domains are interspersed with 2D crystallites near the grain boundaries, and we might therefore expect the majority of photo-excited species to be free charge carriers. Terahertz photoconductivity spectra shown in Figure S8 indeed show a Drude-like free-carrier response (positive flat real part, zero imaginary part, as expected for free carriers with short momentum relaxation time) across a range of compositions, indicating that the photoconductivity transients are dominated by the response of free charge carriers in these materials. These results are in good agreement with the photoluminescence and absorption spectra that we measure (Figure S1), and by the typical transient photoconductivity decays observed (Figure S9), which are close to those measured previously for 3D bulk perovskites.[11,38,40,41]

Optical-Pump Terahertz-Probe Spectroscopy

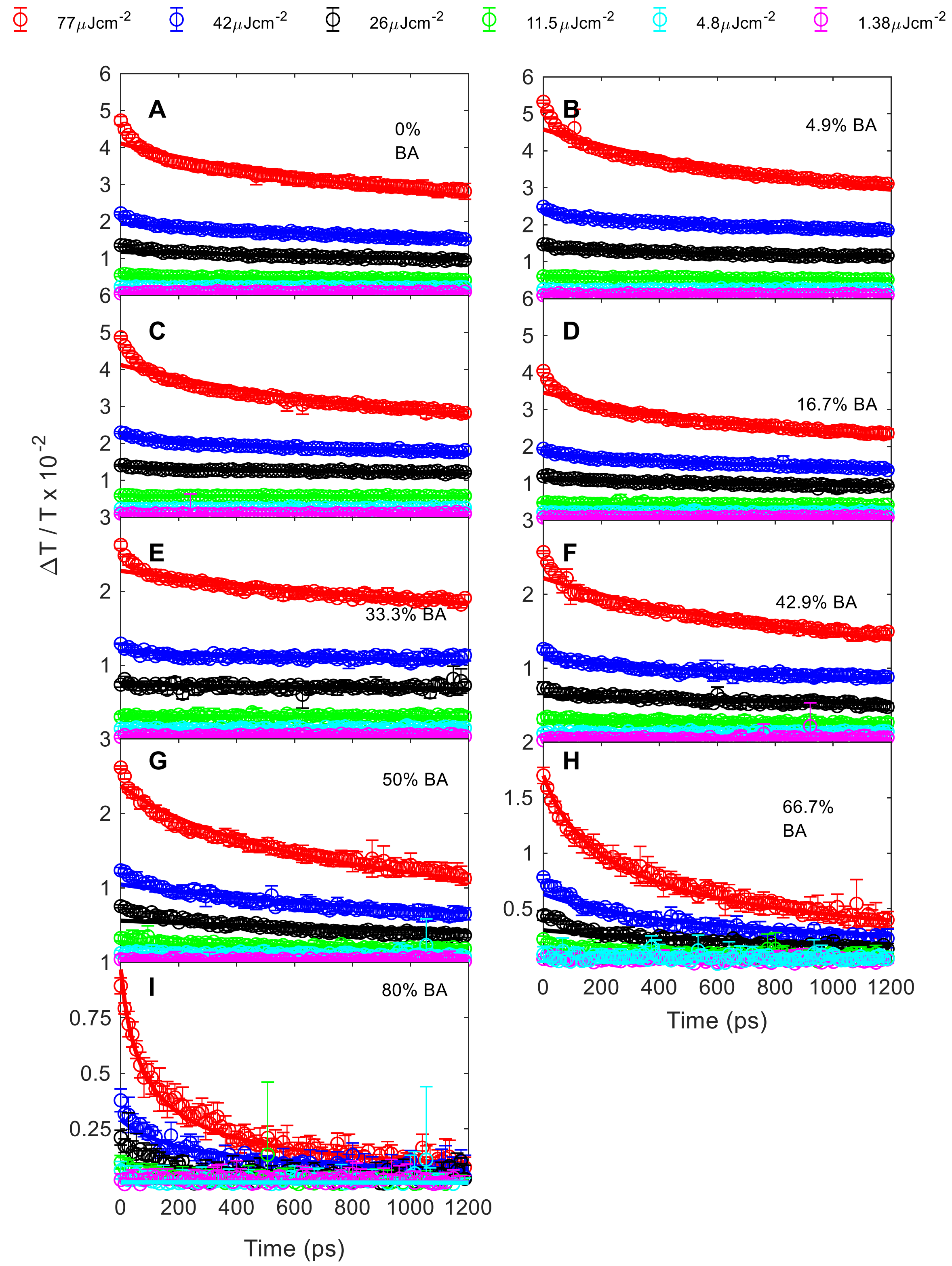

Figure S9: (A) – (I) Optical-Pump, THz-probe transient decay traces for thin films of $BA_x(FA_{0.83}Cs_{0.17})_{1-x}Pb(I_{0.6}Br_{0.4})_3$, measured following excitation at 400nm at a range of fluences for 0 – 0.8 BA content. Data points are in open circles with error bars, and fits to a standard equation describing the charge-carrier density decay (see below) are solid lines.

Calculation of Charge-Carrier Mobility

We follow the same process outlined by Wehrenfennig et al.[42] Charge-carrier mobility is linked to the photoconductivity of a thin film by:

$$\mu = \frac{\Delta S\, A_{eff}}{Ne} \qquad S1$$

Here ΔS is the sheet conductivity of the film, A_{eff} is the effective overlap area of the optical pump and THz probe beams, *N* is the number of photoexcited free charge carriers, and e is the elementary charge.

Given that THz wavelengths are both much longer than the perovskite film thickness ($\lambda_{THz} \gg d_{film}$), and shorter than the quartz substrate thickness ($\lambda_{THz} < d_{substrate}$), we can use the following approximation for the sheet photoconductivity of a thin film between two media with refractive indeces n_A and n_B:

$$\Delta S = -\epsilon_0 c(n_A + n_B)\left(\frac{\Delta T}{T}\right) \qquad S2$$

Here $\Delta T = T_{excited} - T_{dark}$ is the photoinduced change in THz electric field, and $n_A = 1$ for vacuum and $n_B = 2.13$ for a z-cut quartz substrate.

We determine the number of photoexcited charge-carriers using:

$$N = \phi \frac{E\,\lambda}{h\,c}\left(1 - R_{pump}(\lambda)\right)\left(1 - T_{pump}(\lambda)\right), \qquad S3$$

where E is the energy contained in an optical excitation pulse of wavelength λ (= 400 nm), R_{pump} and T_{pump} are the sample reflectivity and tramittance at 400 nm, and ϕ is the branching ratio of photons-to-free-charges.

We can substitute equations S3 and S2 into S1, in order to obtain:

$$\phi\mu = -\epsilon_0 c(n_A + n_B)\frac{A_{eff} hc}{Ee\lambda\left(1 - R_{pump}(\lambda)\right)\left(1 - T_{pump}(\lambda)\right)}\left(\frac{\Delta \mathrm{T}}{\mathrm{T}}\right) \qquad S4$$

Given that the branching ratio $0 \leq \phi \leq 1$, the calculated effective charge-carrier mobility is always an underestimate; it is only identical to the true free-carrier mobility when there is full conversion of photons to free charges. Further, the determined charge-carrier mobility arises from contributions to the conductivity from both free electrons and free holes, and these cannot be separated. Thus, the effective mobility values given in the main text are the sum of electron and hole mobilities.

For very high excitation fluences (> 50 µJcm^{-2}) the proportionality between $\Delta T\ /\ T$ and μ no longer holds. We thus calculate effective mobilities from the initial $\Delta T\ /\ T$ response for fluences below this value.

Transient Decay Fitting

The overall charge-carrier dynamics in a perovskite semiconductor can be approximately described by the following partial differential equation:

$$\frac{\partial n}{\partial t} = -k_3 n^3 - k^2 n^2 - k_1 n \qquad S5$$

In this case, as we set k$_3$ = 0, the PDE can be solved analytically:

$$\frac{\partial n}{\partial t} = -k^2 n^2 - k_1 n \qquad S6$$

Separating out variables gives us:

$$\int \frac{1}{n\left(1 + \frac{k_2}{k_1} n\right)} \mathrm{d}n = \int -k_1 \mathrm{d}t \qquad S7$$

$$\int \frac{1}{n} - \frac{\frac{k_2}{k_1}}{1 + \frac{k_2}{k_1} n} \mathrm{d}n = \int -k_1 \mathrm{d}t \qquad S8$$

$$\ln(n) - \ln\left(1 + \frac{k_2}{k_1} n\right) = -k_1 t + A, \qquad S9$$

$$\ln\left(\frac{n}{1 + \frac{k_2}{k_1} n}\right) = -k_1 t + A, \qquad S10$$

where A is simply the integration constant. Then, exponentiating both sides:

$$\frac{n}{1+\frac{k_2}{k_1}n} = B\mathrm{e}^{-\mathrm{k}_1 t}\,, \qquad S11$$

where $B = e^A$, another constant. Thus, rearranging for n:

$$n(t) = \frac{B}{e^{k_1 t} - \frac{k_2}{k_1}B} \qquad S12$$

Finally, substituting in for $\alpha = \frac{B}{k_1}$:

$$n(t) = \frac{k_1\alpha}{e^{k_1 t} - k_2\alpha} \qquad S13$$

We can relate α to the initial charge-carrier density n_0 via:

$$\frac{1}{\alpha} = \frac{k_1}{n_0} + k_2 \qquad S14$$

Thus, at $t = 0$, we recover $n(t = 0) = n_0$.

The change in transmitted THz radiation $\Delta T\ /\ T\ (t) \equiv x(t)$ is proportional to the free charge-carrier density in the thin film:

$$n(t) = \phi\, C\, x(t) \qquad S15$$

Here ϕ indicates the number of free charge-carriers generated per photon, and $C = \tilde{n}_0\ /\ x(0)$ is the proportionality factor between the initial THz response $x(0)$ and the absorbed photon density $\tilde{n}_0$, given by:

$$\tilde{n}_0 = \frac{E\,\lambda\,\alpha(\lambda)}{h\,c\,A_{eff}}\left(1 - R_{pump}(\lambda)\right) \qquad S16$$

Here the effective overlap area A_{eff} can be calculated from the pump and probe beam parameters, whilst the absorption and reflection coefficients are measured for each sample. For very high excitation fluences (> 50 µJcm^{-2}) the proportionality in equation S15 no longer holds; we therefore determine C based on the initial response for fluences below this.

Substituting equation S15 into S6 gives us:

$$\frac{\mathrm{d}x}{\mathrm{d}t} = -C\phi k_2 x^2 - k_1 x$$

$$= -A_2x^2 - A_1x \qquad S17$$

Analytical solutions to this ODE are fitted globally to the decays across all fluences in order to extract the rate constants A_i. Given the influence of the photon-to-free-charge conversion ratio ϕ we can only determine apparent bimolecular recombination rates ϕk_2. Just as for the charge-carrier mobility, given that $0 \leq \phi \leq 1$ the values presented for k_2 in the main text are underestimates of the true intrinsic values.

Finally, in order to account for an initial spatially varying charge-carrier density (due to absorption following the Beer-Lambert law), the fitting algorithm takes into account an exponentially decaying charge-carrier density. This is done by dividing the sample into 30 equally thick slices and computing the decay function for each of these individually.

References

[1] T. Seifert, S. Jaiswal, U. Martens, J. Hannegan, L. Braun, P. Maldonado, F. Freimuth, A. Kronenberg, J. Henrizi, I. Radu, E. Beaurepaire, Y. Mokrousov, P. M. Oppeneer, M. Jourdan, G. Jakob, D. Turchinovich, L. M. Hayden, M. Wolf, M. Münzenberg, M. Kläui, T. Kampfrath, *Nat. Photonics* **2016**, *10*, 483.

[2] F. Brivio, A. B. Walker, A. Walsh, *APL Mater.* **2013**, *1*, 042111.

[3] T. Umebayashi, K. Asai, T. Kondo, A. Nakao, *Phys. Rev. B* **2003**, *67*, 155405.

[4] J. M. Frost, K. T. Butler, F. Brivio, C. H. Hendon, M. van Schilfgaarde, A. Walsh, *Nano Lett.* **2014**, *14*, 2584.

[5] J. Even, L. Pedesseau, M. A. Dupertuis, J. M. Jancu, C. Katan, *Phys. Rev. B - Condens. Matter Mater. Phys.* **2012**, *86*, 205301.

[6] J. Even, L. Pedesseau, C. Katan, M. Kepenekian, J. S. Lauret, D. Sapori, E. Deleporte, *J. Phys. Chem. C* **2015**, *119*, 10161.

[7] K. Matsuishi, T. Ishihara, S. Onari, Y. H. Chang, C. H. Park, *Phys. status solidi* **2004**, *241*, 3328.

[8] J. L. Knutson, J. D. Martin, D. B. Mitzi, **2005**, *44*, 4699.

[9] M. R. Filip, G. E. Eperon, H. J. Snaith, F. Giustino, *Nat. Commun.* **2014**, *5*, 5757.

[10] G. E. Eperon, S. D. Stranks, C. Menelaou, M. B. Johnston, L. M. Herz, H. J. Snaith, *Energy Environ. Sci.* **2014**, *7*, 982.

[11] R. L. Milot, G. E. Eperon, H. J. Snaith, M. B. Johnston, L. M. Herz, *Adv. Funct. Mater.* **2015**, *25*, 6218.

[12] A. D. Wright, C. Verdi, R. L. Milot, G. E. Eperon, M. A. Pérez-Osorio, H. J. Snaith, F. Giustino, M. B. Johnston, L. M. Herz, *Nat. Commun.* **2016**, *7*, 11755.

[13] E. S. Parrott, T. Green, R. L. Milot, M. B. Johnston, H. J. Snaith, L. M. Herz, *Adv. Funct. Mater.* **2018**, *28*, 1802803.

[14] P. Nandi, C. Giri, D. Swain, U. Manju, S. D. Mahanti, D. Topwal, *ACS Appl. Energy*

Mater. **2018**, *1*, 3807.

[15] C. Yu, Z. Chen, J. J. Wang, W. Pfenninger, N. Vockic, J. T. Kenney, K. Shum, *J. Appl. Phys.* **2011**, *110*, 063526.

[16] L. D. Whalley, J. M. Skelton, J. M. Frost, A. Walsh, *Phys. Rev. B* **2016**, *94*, 220301.

[17] W. A. Saidi, S. Poncé, B. Monserrat, *J. Phys. Chem. Lett.* **2016**, *7*, 5247.

[18] W. A. Saidi, A. Kachmar, *J. Phys. Chem. Lett.* **2018**, *9*, 7090.

[19] L. Huang, W. R. L. Lambrecht, *Phys. Rev. B* **2013**, *88*, 165203.

[20] J. H. Noh, S. H. Im, J. H. Heo, T. N. Mandal, S. Il Seok, *Nano Lett.* **2013**, *13*, 1764.

[21] L. Protesescu, S. Yakunin, M. I. Bodnarchuk, F. Krieg, R. Caputo, C. H. Hendon, R. X. Yang, A. Walsh, M. V. Kovalenko, *Nano Lett.* **2015**, *15*, 3692.

[22] Z. Wang, Q. Lin, F. P. Chmiel, N. Sakai, L. M. Herz, H. J. Snaith, *Nat. Energy* **2017**, *2*, 17135.

[23] J. Coates, in *Encycl. Anal. Chem.*, **2006**.

[24] G. Ramis, G. Busca, *J. Mol. Struct.* **1989**, *193*, 93.

[25] E. Kucharska, J. Hanuza, A. Ciupa, M. Mączka, L. Macalik, *Vib. Spectrosc.* **2014**, *75*, 45.

[26] J. E. Stewart, *J. Chem. Phys.* **1959**, DOI 10.1063/1.1730168.

[27] E. M. Layton, R. D. Kross, V. A. Fassel, *J. Chem. Phys.* **1956**, *25*, 135.

[28] Y. Wang, R. A. Poirier, *J. Phys. Chem. A* **1997**, DOI 10.1021/jp9617332.

[29] L. M. Herz, *Annu. Rev. Phys. Chem.* **2016**, *67*, 65.

[30] M. B. Johnston, L. M. Herz, *Acc. Chem. Res.* **2016**, *49*, 146.

[31] M. Hirasawa, T. Ishihara, T. Goto, K. Uchida, N. Miura, *Phys. B Condens. Matter* **1994**, *201*, 427.

[32] K. Tanaka, T. Takahashi, T. Ban, T. Kondo, K. Uchida, N. Miura, *Solid State Commun.* **2003**, *127*, 619.

[33] S. D. Stranks, G. E. Eperon, G. Grancini, C. Menelaou, M. J. P. Alcocer, T. Leijtens, L.

M. Herz, A. Petrozza, H. J. Snaith, *Science* **2013**, *342*, 341.

[34] C. Wehrenfennig, G. E. Eperon, M. B. Johnston, H. J. Snaith, L. M. Herz, *Adv. Mater.* **2014**, *26*, 1584.

[35] C. S. Ponseca, T. J. Savenije, M. Abdellah, K. Zheng, A. Yartsev, T. Pascher, T. Harlang, P. Chabera, T. Pullerits, A. Stepanov, J.-P. Wolf, V. Sundström, *J. Am. Chem. Soc.* **2014**, *136*, 5189.

[36] Y. Yamada, T. Nakamura, M. Endo, A. Wakamiya, Y. Kanemitsu, **2014**, DOI 10.1021/JA506624N.

[37] R. L. Milot, M. T. Klug, C. L. Davies, Z. Wang, H. Kraus, H. J. Snaith, M. B. Johnston, L. M. Herz, *Adv. Mater.* **2018**, *30*, 1804506.

[38] R. L. Milot, R. J. Sutton, G. E. Eperon, A. A. Haghighirad, J. Martinez Hardigree, L. Miranda, H. J. Snaith, M. B. Johnston, L. M. Herz, *Nano Lett.* **2016**, *16*, 7001.

[39] H. Tsai, W. Nie, J.-C. Blancon, C. C. Stoumpos, R. Asadpour, B. Harutyunyan, A. J. Neukirch, R. Verduzco, J. J. Crochet, S. Tretiak, L. Pedesseau, J. Even, M. A. Alam, G. Gupta, J. Lou, P. M. Ajayan, M. J. Bedzyk, M. G. Kanatzidis, A. D. Mohite, *Nature* **2016**, *536*, 312.

[40] W. Rehman, D. P. Mcmeekin, J. B. Patel, R. L. Milot, M. B. Johnston, H. J. Snaith, L. M. Herz, *Energy Environ. Sci. Energy Environ. Sci* **2017**, *10*, 361.

[41] T. W. Crothers, R. L. Milot, J. B. Patel, E. S. Parrott, J. Schlipf, P. Mü Ller-Buschbaum, M. B. Johnston, L. M. Herz, *Nano Lett.* **2017**, *17*, 5782.

[42] C. Wehrenfennig, M. Liu, H. J. Snaith, M. B. Johnston, L. M. Herz, *Energy Environ. Sci.* **2014**, *7*, 2269.